IEEE Access
Multidisciplinary ⋮ Rapid Review ⋮ Open Access Journal

Received 12 May 2023, accepted 3 June 2023, date of publication 7 June 2023, date of current version 14 June 2023.

Digital Object Identifier 10.1109/ACCESS.2023.3283921

RESEARCH ARTICLE

Analysis and Experimental Verification of the EMI Signature of Three-Phase Three-Level TCM Soft-Switching Converter Systems

SPASOJE MIRIC[1], (Member, IEEE), PASCAL S. NIKLAUS[2], (Member, IEEE), JONAS HUBER[2], (Senior Member, IEEE), CHRISTOF STÄGER[2], MICHAEL HAIDER[2], AND JOHANN W. KOLAR[2], (Fellow, IEEE)

[1]Innsbruck Drive and Energy Systems Laboratory, University of Innsbruck, 6020 Innsbruck, Austria
[2]Power Electronic Systems Laboratory, ETH Zürich, 8092 Zürich, Switzerland

Corresponding author: Jonas Huber (huber@lem.ee.ethz.ch)

ABSTRACT This paper investigates the Electromagnetic Interference (EMI) noise signature of three-phase three-level (3L) Triangular Current Mode (TCM)-modulated grid-tied Photovoltaic (PV) inverters that achieve full Zero Voltage Switching (ZVS) and thus minimal switching losses over the entire mains period and/or ensure $> 99\,\%$ efficiency. Further required is a very high power density, which facilitates installation and is achieved with high switching frequencies $> 100\,\text{kHz}$. The impact of the characteristic variation of f_{sw} in all three phases and the therefore different instantaneous switching frequencies in each phase on the overall converter EMI noise signature is analyzed and it is found that the consideration of only one single phase is sufficient to characterize the noise emissions. Numeric approaches to estimate the detector output of EMI test receivers are compared and it turns out that the peak value of the noise voltage envelope is a useful measure to determine the required filter attenuation, provided the phase-shift of the harmonics is considered in the envelope detection. Finally, a hardware demonstrator of a 6.6 kW, $> 99\%$ efficiency three-phase 3L-TCM PV inverter with a power density of $6.2\,\text{kW/dm}^3$ ($102\,\text{W/in}^3$) is designed and the theoretical findings are verified. Moreover, the impact of parasitic capacitances from the switch-nodes and from the floating dc link to Protective Earth (PE) is thoroughly studied qualitatively and quantitatively with the result that these capacitances considerably reduce filter attenuation (35 dB at 150 kHz in the case at hand), requiring sufficient design margin.

INDEX TERMS Electromagnetic interference (EMI), triangular current mode (TCM), inverter, dc-to-ac converter, soft switching, zero voltage switching (ZVS).

I. INTRODUCTION

Modern renewable energy sources such as wind and solar power are pivotal to limit the global temperature rise to 1.5 °C above pre-industrial levels [1] according to the "Net Zero Emissions by 2050 Scenario (NZE)". To achieve this, their share of the total consumed energy must increase from 11.5% (in 2019; including hydro power) to 32% in 2030 [2], [3]. PV inverters that interface solar panels with the public three-phase grid play a central role in this transition. Given the vast amount of currently and prospectively installed inverters, a very high power density and system efficiency is required. The former is achieved with high switching frequencies f_{sw} to reduce the value and volume of filtering elements ensuring compliance with EMI regulations, whereas the latter demands for Soft Switching (SSW) operation [4] to ensure low switching losses despite elevated switching frequencies. In this regard, TCM operation [5] (sometimes also denoted Critical Conduction Mode (CRM)) has been proposed in order to achieve full ZVS [6] over the entire mains period,

The associate editor coordinating the review of this manuscript and approving it for publication was Pinjia Zhang.

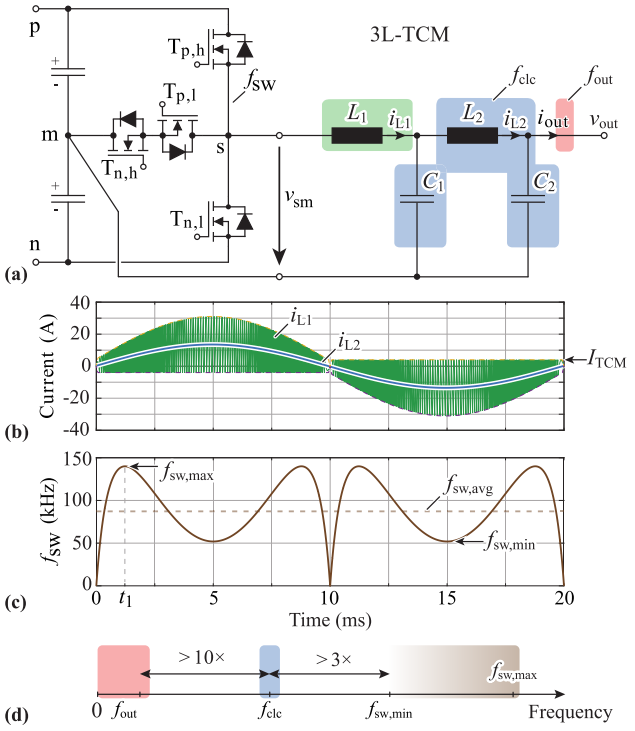

FIGURE 1. **(a) Single-phase 3L T-type bridge-leg of the investigated PV inverter operated with TCM modulation, including the 2-stage *LC* EMI output filter. (b) Characteristic TCM current waveform (i_{L1}) and filtered current (i_{L2}) including the required TCM current I_{TCM} to enable ZVS in every switching transition. (c) Resulting switching frequency variation over one mains period including the average f_{sw} (dashed). (d) Required frequency separation for the design of the output filter to not excite filter resonances and to leave some control margin.**

particularly in single-phase Power Factor Correction (PFC) rectifiers [7], [8], [9] but also in three-phase rectifiers [10], inverters [11], [12], [13], [14] or bidirectional converters [15], [16]. Characteristic for TCM is a large inductor current ripple, which on the one hand minimizes the filter inductor value and volume and on the other hand reverses the current flow direction at the end of each switching pulse interval to enable ZVS for the high-side and low-side transistors in a half-bridge configuration. The large current ripple leads to slightly increased semiconductor conduction losses of around 30% compared to a purely sinusoidal fundamental frequency current [17], which is, however, overcompensated by the substantial reduction of switching losses for high switching frequencies, thereby allowing the desired operation at f_{sw} above 100 kHz to maximize power density. At the same time, f_{sw} locally varies over one mains period, which renders EMI filter design challenging [9], [18], particularly if the occurring maximum value $f_{sw,max}$ falls within the regulated conducted emissions band starting at 150 kHz [19]. By providing a three-level (3L) voltage at the switch-node, i.e., by more closely representing the desired sinusoidal output voltage waveform, e.g., by means of a T-type converter structure [20] as shown in Fig. 1 **(a)** for one phase leg of the considered three-phase 3L-TCM PV inverter, the variation of f_{sw} can be reduced and a further volume reduction of the filtering elements is achieved [21]. In contrast to other realizations that include phase-coupled filters [12], [15], [16], the filter capacitors C_1 and C_2 of the two-stage *LC* output filter are connected to the dc-link midpoint 'm', which gives a fully phase-modular converter structure that, e.g., facilitates economies of scale, has lower complexity of manufacturing and control, and allows operation also with only one or two grid phases. Moreover, simultaneous filtering of Differential Mode (DM) *and* Common Mode (CM) EMI noise components is achieved, while the CM filtering/attenuation can be further improved by means of small toroidal cores placed on the output phase connections (''plug-on choke''), which again simplifies manufacturing and facilitates scalability. The characteristic TCM inductor (L_1) current waveform is depicted in Fig. 1 **(b)** together with the resulting switching frequency variation inherent to TCM operation in Fig. 1 **(c)**.

There exist alternative concepts to achieve full ZVS with the help of auxiliary resonant circuits at the switch-node [21], [22], in the bridge-leg [23], [24] or on the dc-link side [25], [26]. However, employing additional circuits—apart from the additional hardware effort—typically requires precise timing and results in a complex control implementation compared to TCM modulation, which simply adjusts the timing of the switching instants and does not require any additional circuitry [21].

There are fundamental differences regarding the EMI noise signature between TCM-operated converters and systems operated with conventional Pulse Width Modulation (PWM). The inherent f_{sw} variation of the former naturally spreads the total noise energy over a wide frequency range (similar to spread-spectrum modulation [27]), which can be beneficial to comply with regulatory conducted emissions Electromagnetic Compatibility (EMC) standards such as CISPR 11 (EN 55011) [19], whereas the latter shows noise spurs at multiples of f_{sw} (and the respective sidebands), corresponding to a concentration of the noise energy at distinct frequencies. The EMI signature of single-phase TCM rectifiers and inverters has been comprehensively analyzed in literature [21], [28], however, the very important implications of having three bridge-legs—each with variable f_{sw}, i.e., at every point in time (e.g., during one fundamental/mains period) three different switching frequencies $f_{sw,a}$, $f_{sw,b}$ and $f_{sw,c}$ are occurring in phases *a*, *b* and *c*—on the overall noise emissions have not been studied so far. In this paper, first basic filter design guidelines based on the TCM operation are provided in Section. II. Based on the operating principle of EMI test receivers, Section. III then analyzes and compares the EMI signature of a three-phase 3L-TCM inverter (i) by considering only one single phase and (ii) by simultaneously considering all three phases by means of a decomposition into CM and DM noise components. Finally, a hardware demonstrator of a 6.6 kW three-phase 3L-TCM PV inverter according to the specifications listed in Table. 1 is presented and

TABLE 1. Specifications of the considered three-phase 3L-TCM PV inverter.

Description	Parameter	Value
Output Voltage Amplitude	$\hat{v}_{\text{out}}$	325 V
Output Current Amplitude (per Phase)	$\hat{i}_{\text{out}}$	13.5 A
Output Power	P_{out}	$3 \times$ 2.2 kW
Output Frequency	f_{out}	50 Hz
Grid Reactive Power	Q_{g}	10% of P_{out}
DC-Link Voltage	V_{dc}	800 V
ZVS Current	I_{TCM}	4 A
Max. Switching Frequency	$f_{\text{sw,max}}$	140 kHz
EMI Compliance Standard	CISPR 11 Class A	

measurements verify compliance with regulatory standards on conducted emissions. Thereby, the influence of parasitic switch-node capacitances is thoroughly investigated.

II. TCM OPERATION AND FILTER DESIGN

The variable switching frequency of TCM-operated converters results from the non-linear hysteresis control where the switching actions are invoked when the inductor current reaches the predefined minima and maxima of the desired envelope, hence ensuring the required polarity reversal in each switching pulse interval as well as the correct average current value to deliver the desired output power (cf. Fig. 1 **(b)**). The choice of L_1 is critical as it defines the current envelope as well as the occurring f_{sw} variation (cf. Fig. 1 **(c)**) during one mains period, where the maximum value $f_{\text{sw,max}}$ has to be constrained to values below 150 kHz. For a given $f_{\text{sw,max}}$ and modulation index $M = 2\hat{v}_{\text{out}}/V_{\text{dc}}$, it is found as

$$L_1 = \frac{V_{\text{dc}}}{4 f_{\text{sw,max}}} \cdot \frac{M \sin(\omega t_1) \cdot [1 - M \sin(\omega t_1)]}{\hat{i}_{\text{out}} \sin(\omega t_1) + I_{\text{TCM}}}, \quad (1)$$

where the $\hat{v}_{\text{out}}$ and $\hat{i}_{\text{out}}$ are the amplitudes of the output voltage and current, ω is the grid frequency as defined in Table. 1 and I_{TCM} is the required negative current to achieve full ZVS,[1] determined based on the semiconductor output capacitances [17], [29]. As calculated in [21], the time instant t_1 where the maximum switching frequency $f_{\text{sw,max}}$ occurs is given by

$$\sin(\omega t_1) = \frac{\sqrt{I_{\text{TCM}}\left(\hat{i}_{\text{out}} + M I_{\text{TCM}}\right)} - \sqrt{M} I_{\text{TCM}}}{\sqrt{M}\hat{i}_{\text{out}}}. \quad (2)$$

With the specifications in Table. 1, $L_1 = 36\,\mu\text{H}$ results, independent of the output current (part-load operation), i.e., the current ripple amplitude always stays the same and the f_{sw} variation does not change for part-load operation, facilitating EMI filter design.[2] The remaining filter components (*CLC* filter, highlighted in blue in Fig. 1 **(a)**) have to be dimensioned in order to fulfill the EMI regulations. Thereby, full phase modularity is assumed (valid assumption as verified in Section III). The total capacitance $C_{\text{tot}} = C_1 + C_2$ is constrained by the specified maximum grid reactive power consumption $Q_{\text{g}} = 0.1\ P_{\text{out}}$ (10% of the per-phase rated output power, i.e., 0.22 kVAr), hence, $C_{\text{tot}} \leq 2\ Q_{\text{g}}/(\omega \hat{v}_{\text{out}}^2) = 13.2\,\mu\text{F}$. Selecting $C_1 = C_2 = 6.6\,\mu\text{F}$ maximizes filter attenuation for a given C_{tot} and finally, L_2 follows from the required filter resonance frequency $f_{\text{clc}} = 1/(2\pi\sqrt{L_2 C_{12}})$ with $C_{12} = C_1 C_2/(C_1 + C_2)$ to achieve the required attenuation. The filter resonance must be constrained to $f_{\text{clc}} < f_{\text{sw,min}}/3$ and $f_{\text{clc}} > 10 f_{\text{out}}$ to prevent exciting the filter resonances and to provide sufficient control margin (cf. Fig. 1 **(d)**). Thus, f_{clc} is either constrained by the required filter attenuation or by the demanded frequency separation.[3]

III. EMI NOISE ANALYSIS

First, the frequency spectrum of the noise source must be characterized and at each frequency, the difference between noise voltage and regulatory limit (weighted according to the EMI test receiver detector as explained in the following section) corresponds to the required filter attenuation Att_{req}. To determine the noise voltage spectrum, one can (i) examine all three phases simultaneously and separately consider the CM component $v_{\text{cm}} = 1/3 \sum_i v_{\text{sw},i}$, $i = \{\text{a, b, c}\}$ and DM components $v_{\text{dm},i} = v_{\text{sw},i} - v_{\text{cm}}$ with $\sum_i v_{\text{dm},i} = 0$ or (ii) assume full phase modularity and no inter-phase dependencies of the noise voltage spectra, i.e., consider only one single phase (e.g., phase *a*).

Fig. 2 **(a)** shows the three-phase grid-interfaced 3L-TCM inverter with indicated parasitic capacitances from each power semiconductor drain to PE (C_{d}), from the dc-link rails to PE (C_{r}) and from the dc supply midpoint to PE (C_{g}), as well as the EMI filter. The EMI equivalent circuit where the three 3L bridge-legs are replaced with the CM and DM noise voltage sources (based on the modeling approach in [30]) including the two-stage *LC* EMI filter is then shown in Fig. 2 **(b)**. The ac output is connected to a Line Impedance Stabilization Network (LISN) that models a fixed mains impedance of 50 Ω in the conducted emissions frequency range between 150 kHz and 30 MHz ($R_{\text{lisn}} = 50\,\Omega$) and enables noise measurements with help of an EMI test receiver. Moreover, an optional CM choke L_{cm} is included.

[1] Even though the choice of I_{TCM} affects the f_{sw} variation and hence the EMI filter design, because of efficiency considerations it is typically not sensible to select a higher I_{TCM} value than needed for full ZVS.

[2] Alternatively, the current envelope could be narrowed for part-load operation (while still reaching I_{TCM} for achieving ZVS), thus resulting in lower conduction losses and better part-load efficiency but potentially adversely impacting EMI filter design due to concentration of spectral energy at distinct frequencies ($f_{\text{sw,max}}$ and harmonics), similar to conventional PWM.

[3] If no filter design is found that fulfills both criteria, a higher-order filter structure must be employed.

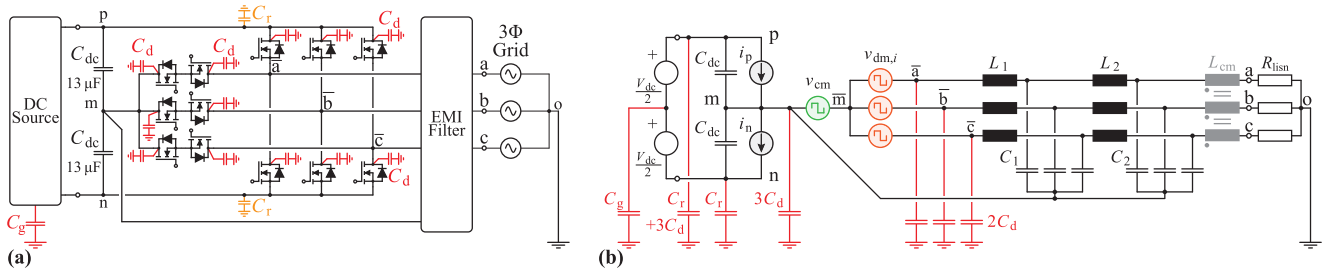

FIGURE 2. (a) Three-phase 3L-TCM PV inverter and (b) its corresponding EMI equivalent circuit including parasitic drain capacitances C_d from each power semiconductor to PE as well as parasitic or desired capacitances C_r from the dc-link rails to PE and additionally a capacitance C_g modeling either the isolation capacitance of dc supplies or the capacitance of PV panels to PE. Further included is an optional CM choke L_{cm} at the phase output connections.

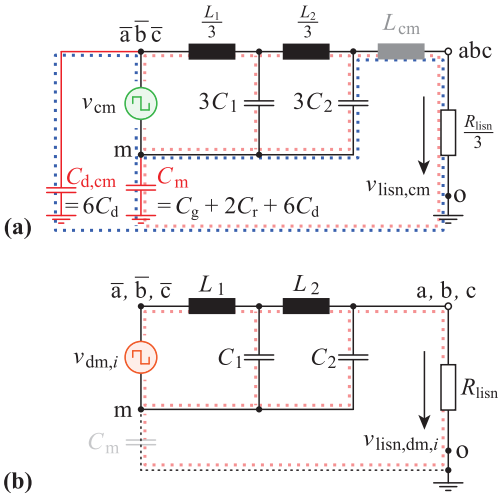

FIGURE 3. (a) CM and (b) DM equivalent circuit resulting from Fig. 2. Indicated are the current paths of the modulation imposed emissions (red) and the parasitically imposed emissions (blue), where the latter are only relevant for CM.

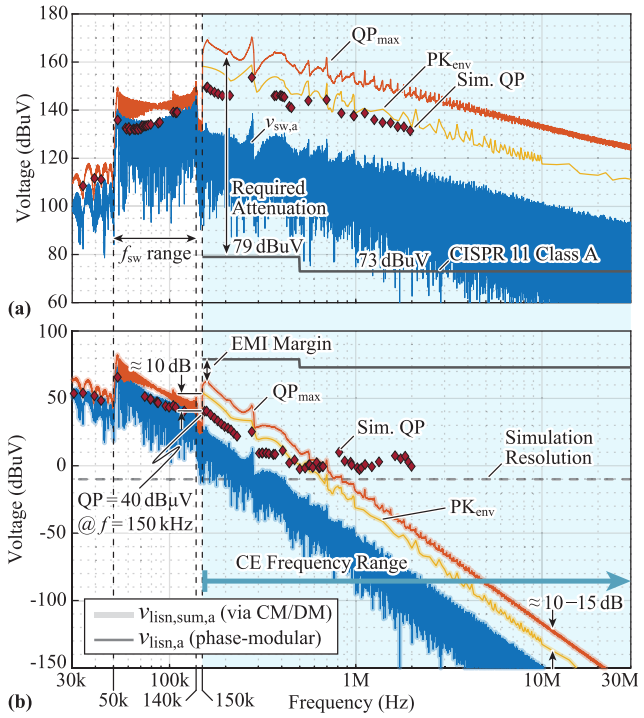

FIGURE 4. Calculated spectra (FFT, blue), worst-case quasi-peak approximation (QP_{max} [31], orange), phase-correct envelope peak estimation (PK_{env} [32], yellow) and simulated quasi-peak detection (time-domain simulation, red diamonds) of (a) the switch-node voltage $v_{sw,a}$ and (b) the LISN voltages $v_{lisn,sum,a}$ (thick lines, light color) and $v_{lisn,a}$ (thin lines) where the former is determined using a CM/DM decomposition of the three-phase switch-node voltage and the CM and DM equivalent filter transfer functions and the latter is determined in a phase-modular way by considering only one phase voltage. Both curves are identical and lie on top of each other.

A. SIMULTANEOUS THREE-PHASE NOISE CONSIDERATION

Considering first case (i), the respective CM and DM noise voltages result from the calculated switch-node voltage spectrum shown in Fig. 4 **(a)** (blue line, exemplary showing phase *a*; nicely visualizing the distributed spectral energy within the f_{sw} range without dedicated peaks) and separate CM and DM equivalent circuits can be found (Fig. 3 **(a)** and **(b)**). Thereby, the potential impact of the three switch-node voltages with different local f_{sw} at every point in time is implicitly included in the CM/DM voltage calculations. As outlined in [33], noise emissions can be categorized into *modulation imposed* (highlighted in red in Fig. 3) and *parasitically imposed* (highlighted in blue in Fig. 3) mechanisms, whereas the latter are defined by the parasitic capacitances C_d, C_r and C_g and can often not be accurately determined during the design stage. From the CM equivalent circuit in Fig. 3 **(a)** follows that the dc-link/midpoint referenced EMI filter composed of $L_1C_1L_2C_2$ cannot effectively filter the parasitically imposed currents that flow through $C_{d,cm} = 6C_d$ (highlighted in blue in Fig. 3 **(a)**), since parts of these currents return through the LISN and C_2 to the midpoint 'm' (the impedance of C_2 in the µF range is much lower [at switching frequency] compared to the impedance of $C_{d,cm}$ and $C_m = C_g + 2C_r + 6C_d$, both in the nF range, and also much lower than the LISN resistance, hence C_2 appears as short-circuit for the return current). Only an additionally placed CM choke L_{cm} provides series impedance and thus reduces the voltage across the LISN measurement resistor. For pure DM noise there is no potential difference between the dc-link midpoint 'm' and the load/grid star point (here PE), thus the two points can be

(virtually) shorted together for the DM analysis (dotted line Fig. 3 **(b)**) and the parasitic capacitances have no influence.

From a *modulation imposed* emissions point of view the shorted connection of 'm' and PE is the worst-case (no voltage drop across C_m, i.e., the voltage across C_2 directly appears at the LISN if L_cm is neglected), whereas for *parasitically imposed* emissions the direct connection ($C_\mathrm{m} = \infty$) is the best-case, since any current flowing through $C_\mathrm{d,cm}$ directly returns to the source without flowing through the LISN. In practice, C_m in a phase-modular converter structure with filter capacitors referenced to the dc-link/midpoint is limited by the maximum allowed ground leakage current of, e.g., $< 9\,\mathrm{mA}$ (rms) (30% of the 30 mA Residual-Current Device (RCD) limit), due to grid voltage imbalances and/or filter capacitor tolerances, which lead to a CM excitation of the midpoint 'm' with respect to PE [34]. Assuming a grid voltage imbalance of ±3%, capacitor tolerances of ±20% and a nominal total per-phase filter capacitance of 13.2µF, C_m must be below 750 nF, which is higher than the typical earth capacitance of standard mono- and polycrystalline solar panels for a power rating of 6.6 kW ($\approx 400 - 730\,\mathrm{nF}$) [35]. Since the parasitic capacitances on the converter (in particular the switch-node capacitances C_d) cannot be accurately determined during the design stage, it is good practice to first consider only the modulation imposed noise emissions and thus assume a direct connection between 'm' and PE. The filter is then designed with sufficient margin to account for the influence of the parasitic capacitances.

EMI test receivers are super-heterodyne mixers [36], which convert the measured input signal with help of a local oscillator at frequency f_lo to a (constant) intermediate frequency f_if around which a so-called Resolution Bandwidth (RBW) filter (bandpass filter with a −6 dB bandwidth of 9 kHz [37]) extracts the relevant frequency content. Afterwards, the envelope x_env of the frequency-selected and bandpass-filtered noise voltage in time-domain is determined before different detectors (average, peak or Quasi-Peak (QP) detectors) weight the shape and repetition rate of x_env to finally end up with the noise voltage quantity that is subject to regulatory limits [32]. This process is repeated for numerous frequency points f_lo between 150 kHz and 30 MHz to cover the full regulated frequency range. There exist limits for the average value $X_\mathrm{avg} = 1/T \int_0^T x_\mathrm{env}(t)\mathrm{d}t$) and the QP value X_QP, which is determined by a lowpass filter with charging time constant $\tau_\mathrm{c} = 1\,\mathrm{ms}$ and discharging time constant $\tau_\mathrm{d} = 160\,\mathrm{ms}$ [37] (non-linear filter), where QP limits for CISPR 11 Class A are indicated in Fig. 4 (dark-gray) and are typically more challenging to fulfill compared to the average limits. The non-linearity of the QP detector makes numerical calculations difficult, hence various approximations and modeling approaches have been presented, such as the so-called QP_max [31], which by adding the magnitudes of all spectral components within the RBW ends up with a conservative estimate of the QP value (in fact QP_max combines envelope detection and QP determination, however more closely estimates the peak value of the envelope, which by definition is always higher or equal than the QP value). Fig. 4 **(a)** shows the QP_max of the switch-node voltage spectrum (orange curve). When considering the phase-shift of the harmonics in addition to their magnitude, x_env can be more accurately determined using a Hilbert transform [32], [38]. The peak value PK_env of this phase-correct envelope is further indicated in Fig. 4 **(a)** (yellow line) and is a more realistic worst-case approximation of the actual QP values determined using circuit simulation in time-domain (red diamonds), whereas QP_max is always $\approx 10 - 15\,\mathrm{dB}$ higher than PK_env. Thus, in case of TCM modulation with spread spectrum, the phase-correct approximation with PK_env is preferably used to estimate the EMI emissions rather than QP_max. Calculations and simulations have shown that in case of conventional sinusoidal PWM the difference between QP_max and PK_env is very small because there is usually only one dominant spectral component within one RBW, hence the phase-shift has practically no influence.

The difference between the estimated QP noise emissions at the switch-node and the respective regulatory limits results in the minimum required filter attenuation at each frequency. In practice, a certain additional margin of $10 - 20\,\mathrm{dB}$ is usually added to account for tolerances of the filter and for influences of parasitic elements such as the previously examined capacitances C_d. According to the CM and DM equivalent circuit, the filter elements have to be scaled to finally determine the emitted noise voltage at the converter terminals, i.e., $v_\mathrm{lisn,cm}$ and $v_\mathrm{lisn,dm,}i$ (cf. Fig. 3 **(a)** and **(b)**), which are then recombined (phase-correct summation) to $v_\mathrm{lisn,sum,}i$, $i = \{a, b, c\}$, exemplary shown for phase a in Fig. 4 **(b)**, again as spectral components (light blue), QP_max (light orange), PK_env (light yellow) and simulated QP values (red diamonds). As mentioned above, a direct connection between midpoint 'm' and PE is assumed, and no parasitic capacitances and no CM choke are included to represent the worst-case for *modulation imposed* emissions.

B. FULLY PHASE-MODULAR NOISE CONSIDERATION

An alternative and potentially simpler way to determine noise emissions is to consider case (ii) with assumed full phase modularity and no inter-phase dependency, i.e., only one single phase (e.g., phase a) is investigated. Only modulation imposed emissions are considered, hence the parasitic capacitances as well as the CM choke are neglected at this point and a short-circuit between 'm' and PE is assumed. Applying the calculated switch-node voltage to the filter model results in the corresponding LISN terminal voltage $v_\mathrm{lisn,a}$ depicted in Fig. 4 **(b)** as spectrum (blue), QP_max (orange) and PK_env (yellow) with thin lines. Evidentially, the calculated LISN voltages for both cases are equal. Thus, for designing a dc-link/midpoint referenced EMI filter in three-phase TCM converters it is sufficient to consider only one single phase. It is again visible that the PK_env approximation

TABLE 2. Main components of the three-phase 3L-TCM hardware demonstrator.

Parameter	Value	Part
Power Semiconductor		
$T_{p,h}$ and $T_{n,l}$	1.2 kV, 16 mΩ, SiC	C3M0016120K [39]
$T_{p,l}$ and $T_{n,h}$	650 V, 15 mΩ, SiC	C3M0015065K [40]
Gate Driver	+2.5/−5 A	UCC27531
Signal Isolator	100 kV/µs, 2.5 kV	IL 711-3E
Filter Inductor L_1	36 µH	12 turns, 420 × 71 µm
Filter Capacitor C_1	6.6 µF, X2 rated	2× B32926C3335K
Filter Inductor L_2	150 µH	25 turns, 0.8 mm
Filter Capacitor C_2	6.6 µF, X2 rated	2× B32926C3335K
Damping Inductor L_{2d}	150 µH	7447706151
Damping Resistor R_{2d}	6.9 Ω	
Control Platform	Xilinx Zynq 7020	TE0720-03-1C

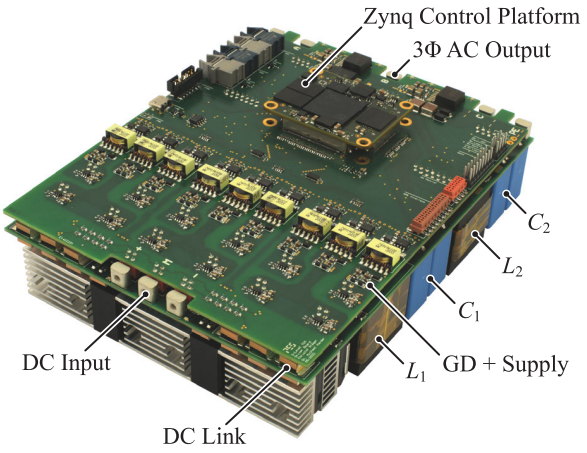

FIGURE 5. Photograph of the hardware prototype with dimensions of 175 mm × 135 mm × 45 mm (6.89 in × 5.31 in × 1.77 in) resulting in a power density of 6.2 kW/dm³ (102 W/in³) and highlighted main building blocks.

more closely matches the simulated QP value compared to the (pessimistic) QP_{max}. Nevertheless, to include sufficient margin, the minimum required attenuation is determined based on QP_{max}, since as mentioned above the influence of parasitic elements (filter self-parasitics and parasitic capacitances of the switch-nodes to PE) are usually not included in the converter design stage but can significantly impact the final filter attenuation as shown in Section. IV-A.

Finally, the resultant filter components to fulfill the regulatory limits are $L_1 = 36\,\mu H$, $C_1 = 6.6\,\mu F$, $L_2 = 150\,\mu H$ and $C_2 = 6.6\,\mu F$. The corner frequency $f_{clc} = 7.2\,kHz$ fulfills both constraints indicated in Fig.1 **(d)** with $f_{sw,min} = 50\,kHz$ and is damped with a series connection of $L_{2d} = 150\,\mu H$ and $R_{2d} = 6.9\,\Omega$ in parallel to L_2 (cf. Table. 2).

IV. HARDWARE DEMONSTRATOR AND EXPERIMENTAL VERIFICATION

To verify the results, an ultra-compact > 99% efficiency hardware demonstrator of the three-phase 3L-TCM inverter is designed and commissioned. From the photograph in Fig. 5 the phase-modular structure can be clearly recognized in the layout. Further highlighted are the most relevant building blocks and components (in particular the filter elements),

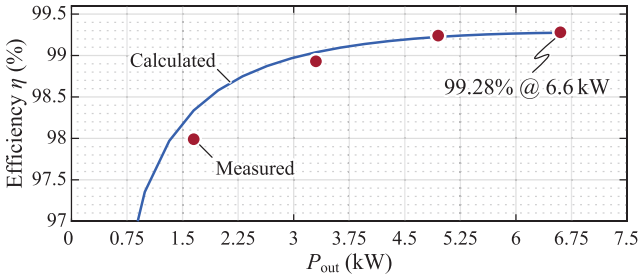

FIGURE 6. Calculated (blue line) and measured (red dots) efficiency of the three-phase 3L-TCM inverter using an ohmic load. Note that both curves do not include the auxiliary power consumption.

which are also listed in Table. 2. The converter volume of 1.06 dm³ (64.8 in³) results in a power density of 6.2 kW/dm³ (102 W/in³). The power semiconductors are equipped with small heat sinks and thanks to the very high efficiency, no forced cooling is required, which is of great advantage considering maintenance and lifetime.

The theoretically calculated and measured efficiencies over the output power range are depicted in Fig. 6 (measurements taken with a Yokogawa WT1800E precision power analyzer) and indicate the achieved target of > 99% full-load efficiency (99.28% at $P_{out} = 6.6\,kW$, i.e., 48 W total losses or 16 W per phase, not considering the auxiliary power consumption in the Watt range, e.g., the driver and measurement circuits and the control circuit). The calculated losses include calorimetrically measured semiconductor switching losses, their conduction losses (ohmic forward conduction and reverse conduction in the internal body diode) and the filter inductor copper and core losses. In addition, a parasitic layout and geometry-related capacitance of $C_{sw} = 200\,pF$ from each phase's switch-node to dc-link potential is included, which leads to additional per-phase switching losses $P_{add} = 0.5\,C_{sw}(V_{dc}/2)^2 f_{sw,avg} = 1.4\,W$ ($f_{sw,avg} = 87.2\,kHz$, cf. Fig. 1 **(c)**).

Fig. 7 **(a)** shows the measured TCM inductor currents (i_{L1}) in all three phases for full-load operation ($P_{out} = 6.6\,kW$) as well as the local variation of f_{sw} in phase b with a maximum value of 140 kHz. Further indicated is the negative current $i_{TCM} = 4\,A$ to facilitate ZVS at every switching instant. The switching operation is temporarily suspended around the zero-crossings (indicated in Fig. 7 **(a)**) because for 3L operation, no current-forming voltage across the inductor L_1 is present at duty-cycles of 50%, and the desired current envelope cannot be tracked. This introduces a certain amount of distortion, which could be mitigated if Hard Switching (HSW) two-level transitions would be allowed during these time intervals, as it is done, e.g., in TCM PFC rectifiers [9]. Note, however, that HSW transitions might slightly increase the EMI emissions in the upper megahertz range due to the typically higher dv/dt compared to SSW transitions.

A. EMI COMPLIANCE VERIFICATION

The blue curve in Fig.7 **(b)** shows the measured conducted EMI noise emissions of phase a under full-load conditions

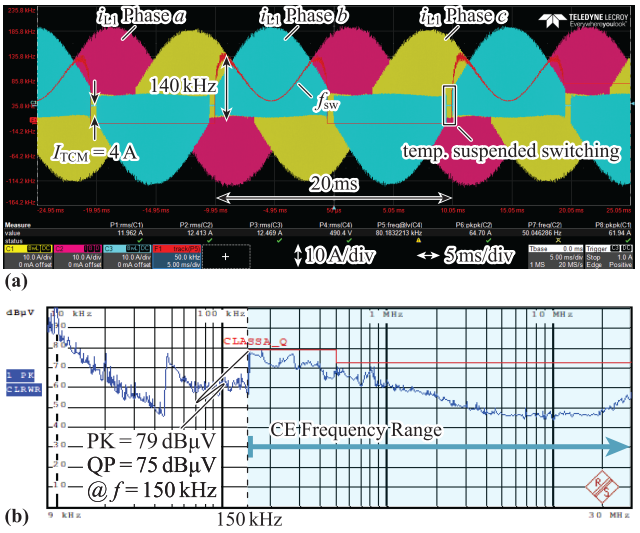

FIGURE 7. (a) Measured waveforms of the TCM inductor current (i_{L1}) of all three phases highlighting the negative current $i_{TCM} = 4$ A to facilitate ZVS and including the measured switching frequency indicating a maximum value $f_{sw,max} = 140$ kHz. (b) Measured EMI spectrum using a peak detector rather than a quasi-peak detector as a worst-case indicator to verify full compliance with CISPR 11 Class A limits. At 150 kHz, the quasi-peak value would be QPK = 75 dBµV whereas the peak detector shows 79 dBµV.

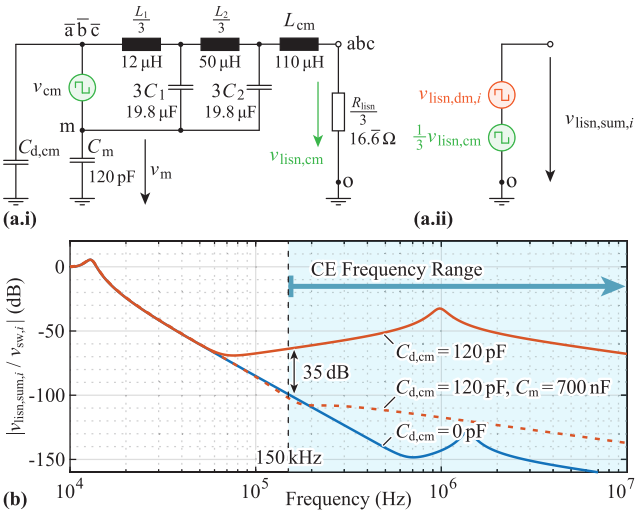

FIGURE 8. (a.i) CM equivalent circuit as shown in Fig. 3 (a) with labeled component values and (a.ii) construction of the final summed LISN noise voltage $v_{lisn,sum,i}$, $i = \{a, b, c\}$ composed of a CM and DM portion. (b) Simulated magnitude response of the transfer function from v_{sw} to the $v_{lisn,sum,i}$, indicating the influence of the switch-node capacitance $C_{d,cm}$ (CM equivalent) and C_m on the filter attenuation, assuming a small CM choke with $L_{cm} = 110$ µH at the three-phase output (three turns on a VAC T60006-L2040-W424 toroidal core).

with a peak detector. The peak detector is a worst-case estimate of the emitted noise but enables significantly faster measurement times (few seconds compared to several hours if the QP detector would be used instead with the same number of frequency points). Due to slight asymmetries in the filter layout and construction of the filter elements, the three phases show somewhat different EMI noise signatures. Phase *a* is depicted as it corresponds to the worst-case. Further indicated are the regulatory CISPR 11 Class A QP limits according to [19] (red line) and it is verified that the system is compliant even with the worst-case peak detector.[4] While the peak detector outputs 79 dBµV at $f = 150$ kHz, the corresponding (measured) QP output is only 75 dBµV.

From the circuit simulation results highlighted with red diamonds in Fig. 4 **(b)** only 40 dBµV (QP value) noise at the output would be expected at $f = 150$ kHz, whereas the experimentally measured QP value is 35 dB higher, i.e., 75 dBµV. The difference can be explained with aforementioned circuit parasitics, particularly the parasitic capacitances from each power semiconductor drain to PE (C_d) and the parasitic capacitances from the dc-link rails to PE (C_r and C_g), which are not considered in the initial filter design procedure from Section. III and are highlighted in the CM equivalent circuit of the noise source and filter structure in Fig. 8 **(a.i)** including their component values. For the measurements the converter is placed without shielding enclosure and the utilized dc supplies (two series-connected Xantrex XDC600-10) are largely decoupled with CM chokes, as otherwise the intrinsically emitted CM noise at their dc output terminals would already exceed the regulatory limits. Therefore, the effective capacitance C_m from the dc-link midpoint to PE is composed solely of six parasitic drain capacitances ($C_d = 20$ pF per switch is assumed for a floating heat sink installation [33]; three from the switches $T_{p,h}$ and three from the switches $T_{n,h}$), i.e., $C_m = 6C_d = 120$ pF, and does not include the isolation capacitance from the dc supplies to PE. Similarly, each switch-node is composed of two parasitic drain capacitances, hence the CM switch-node capacitance $C_{d,cm} = 6C_d = 120$ pF is included as well. The low ratio $C_m/C_{d,cm} = 1$ and high ratio $Z_{C_m}/(R_{lisn}/3) \approx 530$ ($C_m = 120$ pF correspond to 8.8 kΩ at 150 kHz) result in a considerable (parasitically imposed) CM noise voltage v_m across C_m (indicated in Fig.8 **(a.i)**) and hence across the series combination of LISN and L_{cm} and of course across the LISN itself ($v_{lisn,cm}$; again assuming $3C_2$ acting virtually as short-circuit for $f \geq 150$ kHz, since $|Z_{C=19.8\mu F@150\,kHz}| = 0.054\,\Omega \ll R_{lisn}/3$). Fig. 8 **(b)** visualizes the resulting simulated LISN voltage $v_{lisn,sum,i}$ normalized to a noise emission v_{sw} and thereby the degradation of the attenuation for the filter designed according to the procedure outlined in Section. III, if the parasitic switch-node capacitance $C_{d,cm}$ is considered (orange curve) compared to the idealized case without $C_{d,cm}$ (blue curve). The indicated LISN voltage accounts for the influence of the parasitic capacitances only on the CM portion and not on the DM portion of the emissions, i.e., $v_{lisn,sum,i}$ is composed of a CM (green) and DM (orange) part (cf. Fig.8 **(a.ii)**).

At $f = 150$ kHz the impact of the parasitic capacitances on the filter attenuation (degradation by about 35 dB) explains the observed difference of 35 dB between measurement and

[4]It is common practice to perform fast initial measurement using a peak detector and only around frequencies where its output exceeds the regulatory limits use the QP detector, which typically shows a lower output, for a more detailed analysis.

calculation. It also highlights the importance of including sufficient attenuation margin during the filter design stage, in particular if the circuit parasitics are unknown and/or can only be roughly estimated. Here, even a small CM impedance ($L_{cm} = 110\,\mu H$), realized with a single nanocrystalline core (VAC T60006-L2040-W424 from Vacuumschmelze, 43 mm [1.7 in] outside diameter, three turns) placed at the three-phase output terminals, is sufficient to reduce the (CM) emissions below the regulatory limits (see Fig.7 **(b)**; note that a similar CM impedance could also be realized with a single turn and a few more / different cores (''plug-on choke''). From a manufacturability point of view, this is very simple, since no additional PCB-mounted and voluminous component is required and no modification is required to change from three-phase to single-phase operating mode.

Interesting to note is that if a PV array would be used instead of the decoupled dc supply, the now increased C_m of approximately 700 nF and the thereby high ratio $C_m/C_{d,cm} \approx 5800$ and low ratio of $Z_{C_m}/(R_{lisn}/3) \approx 0.1$ ($C_m = 700\,nF$ corresponds to $1.5\,\Omega$ at 150 kHz) would greatly help to improve the attenuation of parasitically imposed emissions as indicated with the dashed line in Fig.8 **(b)**. As mentioned in Section. III, according residual leakage current limits of installed RCDs must be fulfilled and impose an upper limit for C_m.

V. CONCLUSION

Grid-tied high-efficiency Photovoltaic (PV) inverters are instrumental building blocks for the transition to renewable energy sources. To maximize power density, high-frequency Soft Switching (SSW) operation and multi-level switching stages are favorably used, as they allow to minimize the value and size of the dc-link capacitor and input/output filter elements, while still achieving $>$ 99% conversion efficiency. Triangular Current Mode (TCM) modulation thereby ensures full Zero Voltage Switching (ZVS) in every switching transition at the expense of increased conduction losses ($\approx$ 30% higher) and a variable switching frequency (over the mains period). Considering a fully phase-modular three-phase three-level (3L) T-type PV inverter operated with TCM, this paper analyzes the impact of the three instantaneously different switching frequencies in each phase on the overall converter Electromagnetic Interference (EMI) signature. It turns out that it is sufficient to consider solely the emissions of one single phase for the filter design, which greatly facilitates the process. Moreover, it is found that for the occurring spread-spectrum noise emissions, previously utilized approximations for EMI test receiver detectors that consider only the magnitude but not the phase-shift of the spectral components are over-pessimistic, whereas phase-correct envelope detection mechanisms provide a more accurate estimate of the expected EMI signature. Finally, a hardware demonstrator of the investigated 6.6 kW, 99%+ efficiency three-phase 3L-TCM T-type PV inverter with a power density of 6.2 kW/dm^3 (102 W/in^3) is designed to experimentally verify the findings of this paper. Measurements confirm a high efficiency of $>$ 99% over a large range of output power, i.e., 99.28% at full-load (not considering the auxiliary power consumption in the Watt range) as well as full compliance with CISPR 11 Class A EMI limits. Thereby, the influence of converter parasitic capacitances on the achievable filter attenuation is analyzed in detail and it is found that parasitic capacitances from the switch-nodes to Protective Earth (PE), which are typically unknown or very difficult to estimate during the design stage, are particularly critical in combination with dc-link referenced EMI filters, since the resulting Common Mode (CM) currents bypass the installed filter stages. Sufficient filter design margin is therefore required to account for these effects and eventually, already a very small CM inductor (e.g., a single toroidal core placed on the phase output connections) is sufficient to provide the required additional attenuation to comply with the regulatory limits.

REFERENCES

[1] IPCC, ''Summary for policymakers,'' in *An IPCC Special Report on the Impacts of Global Warming of 1.5 °C Above pre-Industrial Levels and Related Global Greenhouse Gas Emission Pathways, in the Context of Strengthening the Global Response to the Threat of Climate Change, Sustainable Development, and Efforts to Eradicate Poverty*, V. Masson-Delmotte, P. Zhai, H.-O. Pörtner, D. Roberts, J. Skea, P. Shukla, A. Pirani, W. Moufouma-Okia, C. Péan, R. Pidcock, S. Connors, J. Matthews, Y. Chen, X. Zhou, M. Gomis, E. Lonnoy, T. Maycock, M. Tignor, and T. Waterfield, Eds. New York, NY, USA: Cambridge Univ. Press, 2018, pp. 3–24. [Online]. Available: https://www.ipcc.ch/site/assets/uploads/sites/2/2022/06/SPM_version_report_LR.pdf

[2] International Energy Agency (IEA). (2021). *World Energy Model*. Accessed: May 3, 2023. [Online]. Available: https://www.iea.org/reports/world-energy-model/

[3] International Energy Agency (IEA). (2022). *SDG7: Data and Projections—Modern Renewables*. Accessed: May 3, 2023. [Online]. Available: https://www.iea.org/reports/sdg7-data-and-projections/modern-renewables

[4] D. Xu, R. Li, N. He, J. Deng, and Y. Wu, *Soft-Switching Technology for Three-Phase Power Electronics Converters*, 1st ed. Hoboken, NJ, USA: Wiley, 2021.

[5] J. G. Cho, D. Y. Hu, and G. H. Cho, ''Three phase sine wave voltage source inverter using the soft switched resonant poles,'' in *Proc. 15th Annu. Conf. IEEE Ind. Electron. Soc.*, Philadelphia, PA, USA, Nov. 1989, pp. 48–53.

[6] C. P. Henze, H. C. Martin, and D. W. Parsley, ''Zero-voltage switching in high frequency power converters using pulse width modulation,'' in *Proc. 3rd Annu. IEEE Appl. Power Electron. Conf. Expo.*, New Orleans, LA, USA, Feb. 1988, pp. 33–40.

[7] Z. Liu, F. C. Lee, Q. Li, and Y. Yang, ''Design of GaN-based MHz totem-pole PFC rectifier,'' *IEEE J. Emerg. Sel. Topics Power Electron.*, vol. 4, no. 3, pp. 799–807, Sep. 2016.

[8] C. Marxgut, J. Biela, and J. W. Kolar, ''Interleaved triangular current mode (TCM) resonant transition, single phase PFC rectifier with high efficiency and high power density,'' in *Proc. Int. Power Electron. Conf.*, Sapporo, Japan, Jun. 2010, pp. 1725–1732.

[9] M. J. Kasper, J. Azurza Anderson, S. Weihe, and G. Deboy, ''Hybrid fixed/variable frequency TCM average current control method enabling ZVS MHz operation of GaN HEMTs in PFC stages,'' in *Proc. IEEE Appl. Power Electron. Conf. Expo. (APEC)*, Orlando, FL, USA, Mar. 2023, pp. 1232–1237.

[10] N. Haryani, B. Sun, and R. Burgos, ''A novel soft switching ZVS, sinusoidal input boundary current mode control of 6-switch three phase 2-level boost rectifier for active and active + reactive power generation,'' in *Proc. IEEE Appl. Power Electron. Conf. Expo. (APEC)*, San Antonio, TX, USA, Mar. 2018, pp. 8–15.

[11] A. Amirahmadi, H. Hu, A. Grishina, Q. Zhang, L. Chen, U. Somani, and I. Batarseh, ''Hybrid ZVS BCM current controlled three-phase microinverter,'' *IEEE Trans. Power Electron.*, vol. 29, no. 4, pp. 2124–2134, Apr. 2014.

[12] J. Chen, D. Sha, J. Zhang, and X. Liao, "An SiC MOSFET based three-phase ZVS inverter employing variable switching frequency space vector PWM control," *IEEE Trans. Power Electron.*, vol. 34, no. 7, pp. 6320–6331, Jul. 2019.

[13] N. Haryani, B. Sun, and R. Burgos, "ZVS turn-on triangular current mode (TCM) control for three phase 2-level inverters with reactive power control," in *Proc. IEEE Energy Convers. Congr. Expo. (ECCE)*, Portland, OR, USA, Sep. 2018, pp. 4940–4947.

[14] Z. Huang, Q. Li, and F. C. Lee, "Digital-based soft-switching modulation for high-frequency three-phase inverters with reactive power transfer capability," in *Proc. IEEE Energy Convers. Congr. Expo. (ECCE)*, Portland, OR, USA, Sep. 2018, pp. 6751–6758.

[15] B. Fan, Q. Wang, R. Burgos, A. Ismail, and D. Boroyevich, "Adaptive hysteresis current based ZVS modulation and voltage gain compensation for high-frequency three-phase converters," *IEEE Trans. Power Electron.*, vol. 36, no. 1, pp. 1143–1156, Jan. 2021.

[16] Z. Huang, Z. Liu, F. C. Lee, and Q. Li, "Critical-mode-based soft-switching modulation for high-frequency three-phase bidirectional AC–DC converters," *IEEE Trans. Power Electron.*, vol. 34, no. 4, pp. 3888–3898, Apr. 2019.

[17] M. Haider, J. A. Anderson, N. Nain, G. Zulauf, J. W. Kolar, D. Xu, and G. Deboy, "Analytical calculation of the residual ZVS losses of TCM-operated single-phase PFC rectifiers," *IEEE Open J. Power Electron.*, vol. 2, pp. 250–264, Feb. 2021.

[18] M. Haider, J. A. Anderson, S. Miric, N. Nain, G. Zulauf, J. W. Kolar, D. Xu, and G. Deboy, "Novel ZVS S-TCM modulation of three-phase AC/DC converters," *IEEE Open J. Power Electron.*, vol. 1, pp. 529–543, 2020.

[19] *Industrial, Scientific and Medical Equipment— Radio-Frequency Disturbance Characteristics—Limits and Methods of Measurement*, EN Standard 55011, Apr. 2016.

[20] D. Leuenberger and J. Biela, "Comparison of a soft switched TCM T-type inverter to hard switched inverters for a 3 phase PV grid interface," in *Proc. 15th Int. Power Electron. Motion Control Conf. (EPE/PEMC)*, Novi Sad, Serbia, Sep. 2012, pp. 1–8.

[21] T. Langbauer, S. Miric, M. Haider, J. Huber, and J. W. Kolar, "Comparative evaluation of ARCP and three-level TCM soft-switching bridge-legs for high-frequency SiC converter systems," in *Proc. Int. Power Electron. Conf.*, Himeji, Japan, May 2022, pp. 1734–1741.

[22] M. Lockwood and A. Fox, "A novel high power transistor inverter," in *Proc. Int. Power Electron. Conf.*, Tokyo, Japan, Mar. 1983, pp. 637–648.

[23] T. Sadilek, L. Huber, P. Barbosa, and I. Husain, "Evaluation of split-phase inverter mode for 1-ph/3-ph combo soft-switching PFC for on-board charger applications," in *Proc. IEEE Appl. Power Electron. Conf. Expo. (APEC)*, Orlando, FL, USA, Mar. 2023, pp. 1888–1895.

[24] T. Sadilek, L. Huber, P. Barbosa, and I. Husain, "Investigation of non-unity power factor operation of 3-ph ZVS PFC rectifier for on-board charging of electric vehicles," in *Proc. IEEE Appl. Power Electron. Conf. Expo. (APEC)*, Orlando, FL, USA, Mar. 2023, pp. 1928–1935.

[25] J. Deng, K. Shi, M. Chen, and D. Xu, "Zero-voltage-switching three-phase T-type inverter," in *Proc. IEEE 12th Energy Convers. Congr. Expo.*, Singapore, May 2021, pp. 1909–1915.

[26] J. Deng, C. Hu, K. Shi, M. Chen, and D. Xu, "A ZVS-PWM scheme for three-phase active-clamping T-type inverters," *IEEE Trans. Power Electron.*, vol. 38, no. 3, pp. 3951–3964, Mar. 2023.

[27] F. Pareschi, R. Rovatti, and G. Setti, "EMI reduction via spread spectrum in DC/DC converters: State of the art, optimization, and tradeoffs," *IEEE Access*, vol. 3, pp. 2857–2874, 2015.

[28] T. Liu, Y. Zhang, Z. Wang, C. Chen, and Y. Kang, "Output DM EMI noise prediction for MHz TCM-based single phase inverter," *IEEE Trans. Power Electron.*, vol. 37, no. 12, pp. 14499–14513, Dec. 2022.

[29] M. Kasper, R. M. Burkart, G. Deboy, and J. W. Kolar, "ZVS of power MOSFETs revisited," *IEEE Trans. Power Electron.*, vol. 31, no. 12, pp. 8063–8067, Dec. 2016.

[30] H. Ye, Z. Yang, J. Dai, C. Yan, X. Xin, and J. Ying, "Common mode noise modeling and analysis of dual boost PFC circuit," in *Proc. 26th Annu. Int. Telecommun. Energy Conf.*, Chicago, IL, USA, Sep. 2004, pp. 575–582.

[31] M. L. Heldwein, "EMC filtering of three-phase PWM converters," Ph.D. dissertation, Dept. Inf. Technol. Elect. Eng., ETH Zurich, Zürich, Switzerland, 2008.

[32] L. Yang, S. Wang, H. Zhao, and Y. Zhi, "Prediction and analysis of EMI spectrum based on the operating principle of EMC spectrum analyzers," *IEEE Trans. Power Electron.*, vol. 35, no. 1, pp. 263–275, Jan. 2020.

[33] D. Menzi, D. Bortis, and J. W. Kolar, "EMI filter design for a three-phase buck–boost Y-inverter VSD with unshielded motor cables considering IEC 61800-3 conducted and radiated emission limits," *IEEE Trans. Power Electron.*, vol. 36, no. 11, pp. 12919–12937, Nov. 2021.

[34] U. Stitz, "Leakage currents in power line filters," Schaffner EMV AG, Luterbach, Switzerland, Tech. Rep., 2008.

[35] *Leading Leakage Currents*, SMA Solar Technology, Niestetal, Germany, 2019, pp. 1–7.

[36] W. Schaefer, "Significance of EMI receiver specifications for commercial EMI compliance testing," in *Proc. Int. Symp. Electromagn. Compat.*, Silicon Valley, CA, USA, Aug. 2004, pp. 741–746.

[37] *Specification for Radio Disturbance and Immunity Measuring Apparatus and Methods—Part 1–1: Radio Disturbance and Immunity Measuring Apparatus—Measuring Apparatus*, EN Standard 55016-1-1, Jul. 2019.

[38] A. Bendicks, T. Dörlemann, C. Krause, and S. Frei, "MATLAB/Octave function to evaluate time-domain signals according to the measurement bandwidth and average/peak detector of EMI test receivers," in *Proc. Int. Congr. Expo. Electromag. Compat.*, Cologne, Germany, Jul. 2022, pp. 459–466.

[39] *C3M0016120K—Silicon Carbide Power MOSFET*, Datasheet, Cree, Inc., Durham, NC, USA, 2019.

[40] *C3M0015065K—Silicon Carbide Power MOSFET*, Datasheet, Cree, Inc., Durham, NC, USA, 2022.

SPASOJE MIRIC (Member, IEEE) received the B.Sc., M.Sc., and Ph.D. degrees in electrical engineering from the University of Belgrade School of Electrical Engineering, in 2012, 2013, and 2018, respectively, with a focus on power electronics systems and drives. In 2021, he defended his second Ph.D. thesis with the Power Electronic Systems Laboratory (PES), ETH Zürich, in the advanced mechatronic systems area. More specifically, during the Ph.D. project, he focused on linear-rotary actuator systems with magnetic bearings, resulting in two new machine topologies patented. Since 2021, he has been a Postdoctoral Researcher with PES, with a focus on WBG power converter optimization with hard and soft-switching, new modulation techniques of flying capacitor converters, wireless power transfer systems, and eddy-current-based position sensor systems. He was appointed as an Assistant Professor and the Head of the Innsbruck Drive and Energy Systems Laboratory, University of Innsbruck (UIBK), in January 2023. He proposed a novel self-bearing actuator topology and a generalized complex space vector calculus for linear-rotary machines. He has published more than 20 scientific papers in international journals and conference proceedings and filed seven patents. He has presented two educational seminars at leading international conferences and received five IEEE Transactions and conference prize paper awards.

PASCAL S. NIKLAUS (Member, IEEE) received the M.Sc. (Hons.) and Ph.D. degrees in electrical engineering from ETH Zürich, Switzerland, in 2018 and 2022, respectively. During his studies, he did two internships where he developed hardware, firmware, and software for custom and off-the-shelf test and measurement equipment with duagon AG, Dietikon, Switzerland, as well as working on the firmware development for a new microprocessor architecture with ACP AG, Zürich, Switzerland. In April 2018, he joined the Power Electronic Systems Laboratory (PES), ETH Zürich, as a Ph.D. Student, with a focus on advanced measurement technologies in the field of power electronics and high bandwidth power converters featuring wide-bandgap power semiconductors. Since 2023, he has been a Postdoctoral Researcher with PES, with a research focus on advanced drive systems with wide-bandgap semiconductors, inverters, and electromagnetic interference.

JONAS HUBER (Senior Member, IEEE) received the M.Sc. and Ph.D. degrees from the Swiss Federal Institute of Technology (ETH) Zürich, Switzerland, in 2012 and 2016, respectively. Since 2012, he has been with the Power Electronic Systems Laboratory, ETH Zürich, where he has been a Postdoctoral Researcher, since 2016. Since 2017, he gained industry experience as a Power Electronics Research and Development Engineer with ABB Switzerland, working on high-power dc–dc converter systems for traction applications, and as a Business Development Manager with a Swiss utility company. Then, in 2020, he returned to the Power Electronic Systems Laboratory, as a Senior Researcher. His research interests include solid-state transformers, motor drives, and all types of WBG-semiconductor-based ultra-compact, ultra-efficient, or highly dynamic converter systems.

CHRISTOF STÄGER received the B.Sc. and M.Sc. degrees in electrical engineering and information technology from ETH Zürich, Switzerland, in 2020 and 2022, respectively. During the master's studies, he was a Hardware Design Engineer with the Laboratory for High Power Electronic Systems (HPE), ETH Zürich. After his studies, he joined the Power Electronic Systems Laboratory (PES), ETH Zürich, as a Scientific Assistant. Since December 2022, he has been a Power Electronics Engineer with Bucher Hydraulics, Switzerland, in the field of mobile auxiliary drive systems.

MICHAEL HAIDER received the M.Sc. and Ph.D. degrees in electrical engineering from the Swiss Federal Institute of Technology (ETH) Zürich, Switzerland, in 2017 and 2022, respectively. In 2017, he joined the Power Electronic Systems Laboratory, ETH Zürich, as a Ph.D. Student, with a focus on motor-integrated power factor, corrected single-to-three-phase ac/ac converter concepts. His research interests include synergetically controlled two-stage systems, soft-switching converter topologies, wide-bandgap power semiconductor devices, and their application in next-generation variable speed drive systems.

JOHANN W. KOLAR (Fellow, IEEE) received the M.Sc. and Ph.D. degrees (summa cum laude) from the Vienna University of Technology, Austria, in 1997 and 1999, respectively. Since 1984, he has been an Independent Researcher and an International Consultant in close collaboration with the Vienna University of Technology, in the fields of power electronics, industrial electronics, and high-performance drive systems. He was appointed as an Associate Professor and the Head of the Power Electronic Systems Laboratory, ETH Zurich, in February 2001, and was promoted to the rank of Full Professor, in 2004. He has proposed numerous novel converter concepts, including the Vienna Rectifier, the Sparse Matrix Converter, and the Swiss Rectifier, has spearheaded the development of x-million rpm motors, and has pioneered fully automated multi-objective power electronics design procedures. He has graduated more than 80 Ph.D. students. He has presented more than 30 educational seminars at leading international conferences. He has published more than 1000 journals and conference papers and four book chapters. He has filed more than 200 patents. His current research interests include ultra-compact/efficient WBG converter systems, ANN-based design procedures, solid-state transformers, ultra-high speed drives, bearingless motors, and life cycle analysis of power electronics converter systems. He was elected to the U.S. National Academy of Engineering as an International Member, in 2021. He has received more than 40 IEEE TRANSACTIONS and conference prize paper awards, the 2014 IEEE Power Electronics Society R. David Middlebrook Achievement Award, the 2016 IEEE PEMC Council Award, the 2016 IEEE William E. Newell Power Electronics Award, the 2021 EPE Outstanding Achievement Award, and two ETH Zürich Golden Owl Awards for excellence in teaching. From 2012 to 2016, he served as an IEEE PELS Distinguished Lecturer.